Target thickness studies, run 2 - E06007

Konrad A. Aniol, CSULA

March 10, 2011

Contents

List of Tables

List of Figures

Chapter 1

Synopsis

The targets for run 2 were substantially better than those for run 1. There is no evidence from the raster plots that the beam hit the target ladder. No damage was visible when the targets were dismantled for the thin lead and bismuth targets. The thick lead target showed signs of beam damage. However, for all three targets the counting rates over the raster patterns, divided into 36 regions, were very uniform and independent of beam current. A comparison of the ratio of counting rates in the LHRS for the thin targets agreed within 3% of the ratios expected from a simple quasielastic model proportional to the number of protons per unit area when radiative corrections are applied. The thick lead target produced a yield higher than that expected by about 14% compared to the thin lead target. This enhanced thickness of the thick lead target can be accounted for by material actually accumulating within the raster pattern.

The best measure of the thicknesses for the thin lead and bismuth targets is that found in the measured values from weighing in table 3.3.

Chapter 2

Introduction

E06007, run2, ran, in collaboration with PREX target tests, during the period from January 20, 2008 to January 31, 2008. The beam conditions were somewhat different from the conditions for run1 (March 2007). Settings for the two runs are found at http://hallaweb.jlab.org/experiment/E06-007/. Settings for the left HRS are in table 2.1.

The photograph of the target ladder is in figure 2.1. The top target is the PREX 0.5mm lead target, below that is the thick lead target(0.5mm), then the thin lead target(0.17mm) and at the bottom the bismuth target(0.207mm). The PREX target was perpendicular to the beam and the three targets for E06007 were at 30 degrees with respect to the beam. Cooling was accomplished by conduction from the heavy copper target ladder attached to the liquid hydrogen target above the ladder. In distinction to run 1, no coolant flowed through the target ladder for run 2.

This report uses the same procedures for determining the target thicknesses and target stability for run 2 as the first report on run 1 from September 10, 2010.

`http://www.jlab.org/~aniol/e06007/target-thickness/targ1-thick-report.pdf.`

run period	beam energy GeV	LHRS angle degrees	LHRS momentum GeV/c
March, 2007	2.65236	21.44	2.216
January, 2008	2.77496	20.37	2.34201

Table 2.1: Left HRS settings for the runs of E06007. The beam energy is from Tiefenbach Hall A energy

Figure 2.1: Target ladder for run2. Targets from top to bottom: PREX lead(0.5mm) thick lead(0.5mm), thin lead(0.17mm), bismuth(0.207mm).

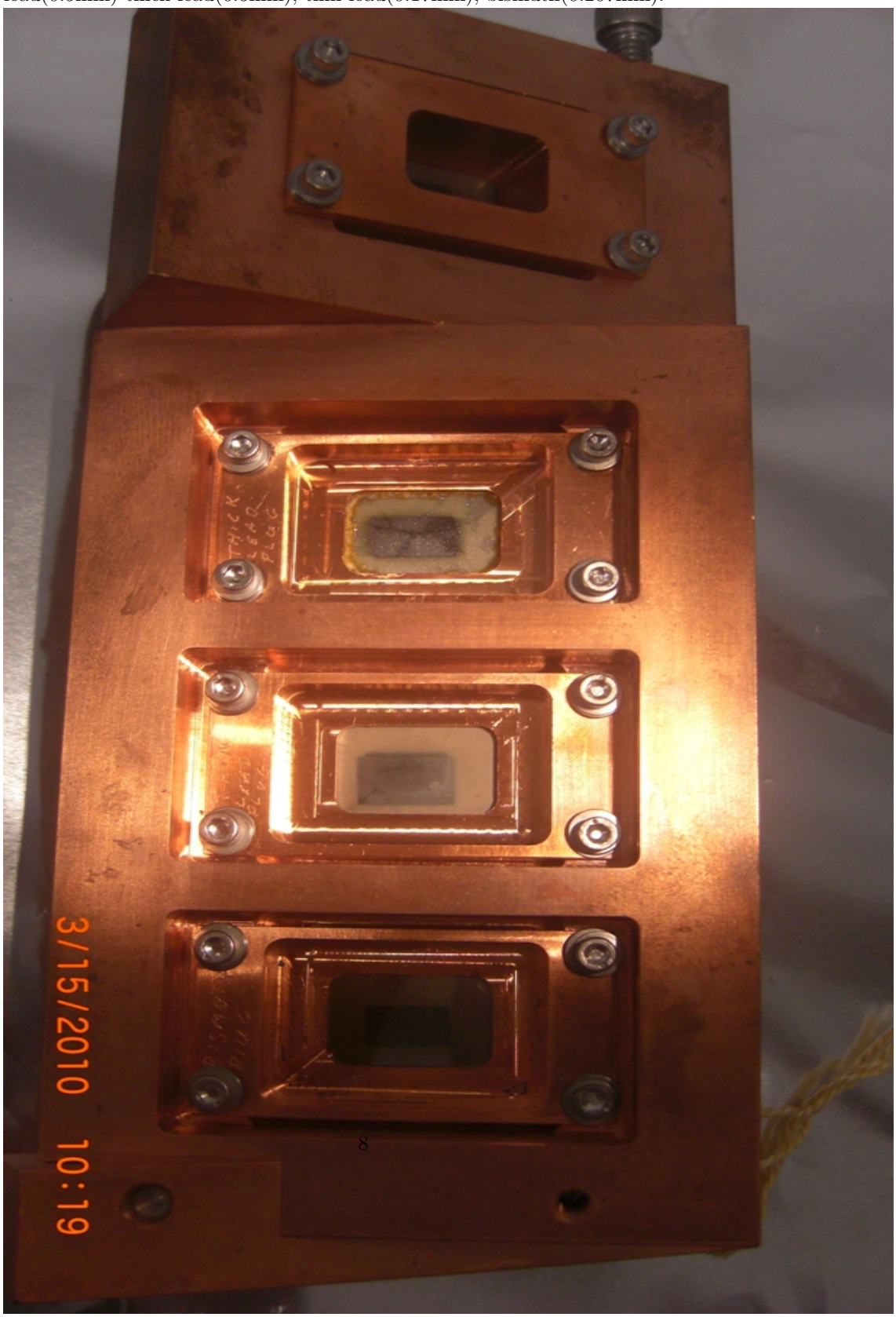

Chapter 3

Initial Target Configurations

The targets as initially installed during run1(March, 2007) and run2(January, 2008) are shown in tables 3.1, 3.2 and 3.3.

foil no.	mass (g)	dimensions inches	mg/cm^2
1	0.3075	0.999x0.999	47.76
2	0.2962	0.998x0.996	46.19
3	0.2989	0.998x0.999	46.47
4	0.2541	0.999x0.999	39.46
5	0.2704	0.998x1.000	42.00
6	0.3366	0.998x1.001	52.23
7	0.3740	0.998x1.001	58.03
8	0.3542	0.998x1.000	55.01
9	0.3122	0.996x0.998	48.86
10	0.3336	0.996x1.000	51.92

Table 3.1: Run 1, March 2007, diamond foils as per Phil Adderley, email June 12, 2008.

ladder position	material 1	material 2	material 3
1	BeO, 149 mg/cm^2		
2	C, 83.8 mg/cm^2		
3	diamond 1 307.5 mg 47.76 mg/cm^2	lead 4, ^{208}Pb 1134 mg 194.8 mg/cm^2	diamond 2 296.2 mg 46.19 mg/cm^2
4	diamond 3 298.9 mg 46.47 mg/cm^2	lead 5, ^{208}Pb 1128 mg 193.7 mg/cm^2	diamond 4 254.1 mg 39.46mg/cm^2
5	diamond 5 270.4 mg 42.00 mg/cm^2	bismuth 1, ^{209}Bi 1320 mg 204.6 mg/cm^2	diamond 6 336.6 mg 52.23 mg/cm^2

Table 3.2: Run 1, March 2007, from Dave Meekins, February 27,2007. Target ladder is tilted at 30 degrees.

target	material	diamond foils no. masses	diamond total mg/cm^2
thick lead no tilt	^{208}Pb, 3314 mg 0.5 mm	11,12 263.7 mg, 292.9 mg	86.34
thick lead 30 deg tilt	^{208}Pb, 3284 mg 0.5 mm	14,16 275.0 mg, 274.2 mg	85.1
thin lead 30 deg tilt	^{208}Pb, 1120 mg 0.17 mm	1,2 316.0 mg, 225.0 mg	83.86
bismuth	^{209}Bi, 1302 mg 0.207 mm 46.47 mg/cm^2	8, 10 354.9mg, 333.5 mg 193.7 mg/cm^2	106.8 39.46mg/cm^2
Carbon 2mm holey			
^{12}C	84.2 mg/cm^2	per email from Meekins	
^{181}Ta	18 mg/cm^2	Jan. 21, 2008	
BeO	149 mg/cm^2		
empty			

Table 3.3: Run 2, January, 2008 from top to bottom. Targets are 1"x1", per Phil Adderley and Dave Meekins.

Chapter 4

Graphite data

The yields in the L.gold.dp spectra are used to determine the target thickness. An example for the graphite target for kin02 is shown in figure 4.1.

An example of a raster pattern for kin02 is shown in figure 4.2. The grid for the matrix of counts per region is displayed in this figure. The raster pattern was very stable during run 2. This figure is typical. There was no evidence that the beam hit the target frame in run2. The 3D raster pattern is displayed in figure 4.3.

Table 4.2 shows the normalized singles rates for graphite. The only kinematic settings where the raster was turned on for the graphite target was kin02.

‘

The counts in the singles spectrum as a function of position in the raster pattern for the graphite target for run 2 is shown in table 4.1. The pattern covers 36 smaller regions.

```
 carbon run 3105, kin02, cutsx(0.008,0.12), cutsy(0.002,0.011)
     y1   y2    y3    y4    y5    y6    y7    y8    y9
x1 0.982 1.000 0.991 0.995 1.000 1.002 1.018 1.018 1.026
x2 0.990 0.968 0.979 0.993 0.998 1.002 1.006 1.025 1.034
x3 0.993 0.981 0.975 0.997 0.990 0.997 0.993 1.027 1.043
x4 0.995 0.978 0.984 0.981 0.991 0.994 0.998 1.033 1.024

avg per bin = 16036.
standard deviation = 295.
sqrt(avg) = 127.
fractional statistical error = 0.008
```

Table 4.1: Graphite, kin02 r3105 raster pattern with matrix to determine target uniformity. The counts are normalized to the average of the bins.

kin	run number	target	current μ A	raster fraction	LHRS singles, normalized $\times 10^7$
kin02	3104	C-off	52	NA	4.887
	3105	C-on	58	0.303	4.916
	3105	C-on	58	1.0	4.872
kin10	3204	C-off	1.8	NA	4.855
kin11	3298	C-off	6.0	NA	4.905

Table 4.2: Normalized LHRS singles counts for rastered and unrastered beam for the graphite target. $\theta_L = 20.37°$, $P_L = 2.34201 GeV/c$, Tiefenbach Hall A energy = $2.77496 GeV$. The normalized singles counts is counts/Coulomb.

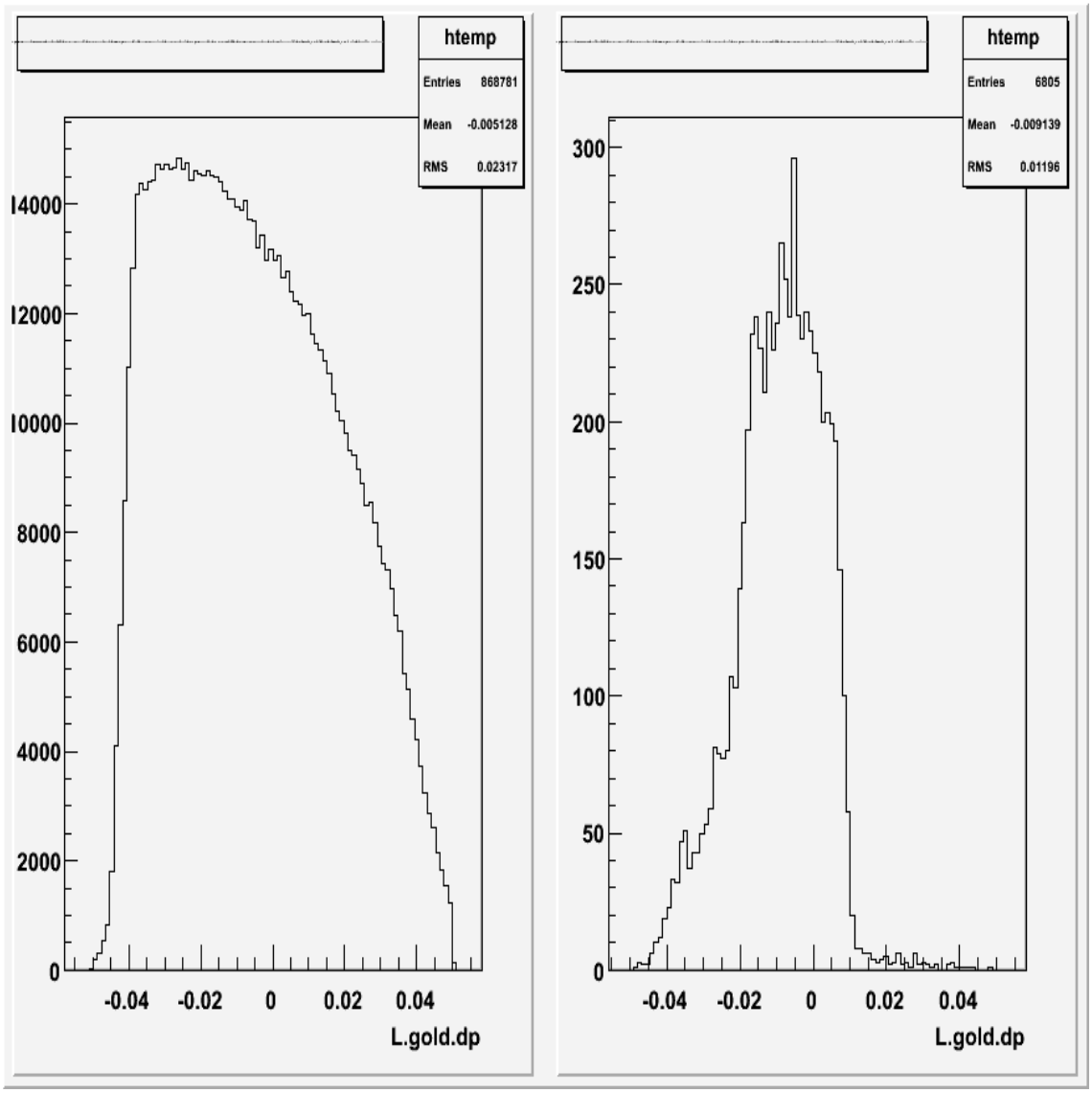

Figure 4.1: Singles spectrum L.gold.dp and coincidence spectrum for the graphite target, run2. Spectra are for the full raster pattern, run 3105.

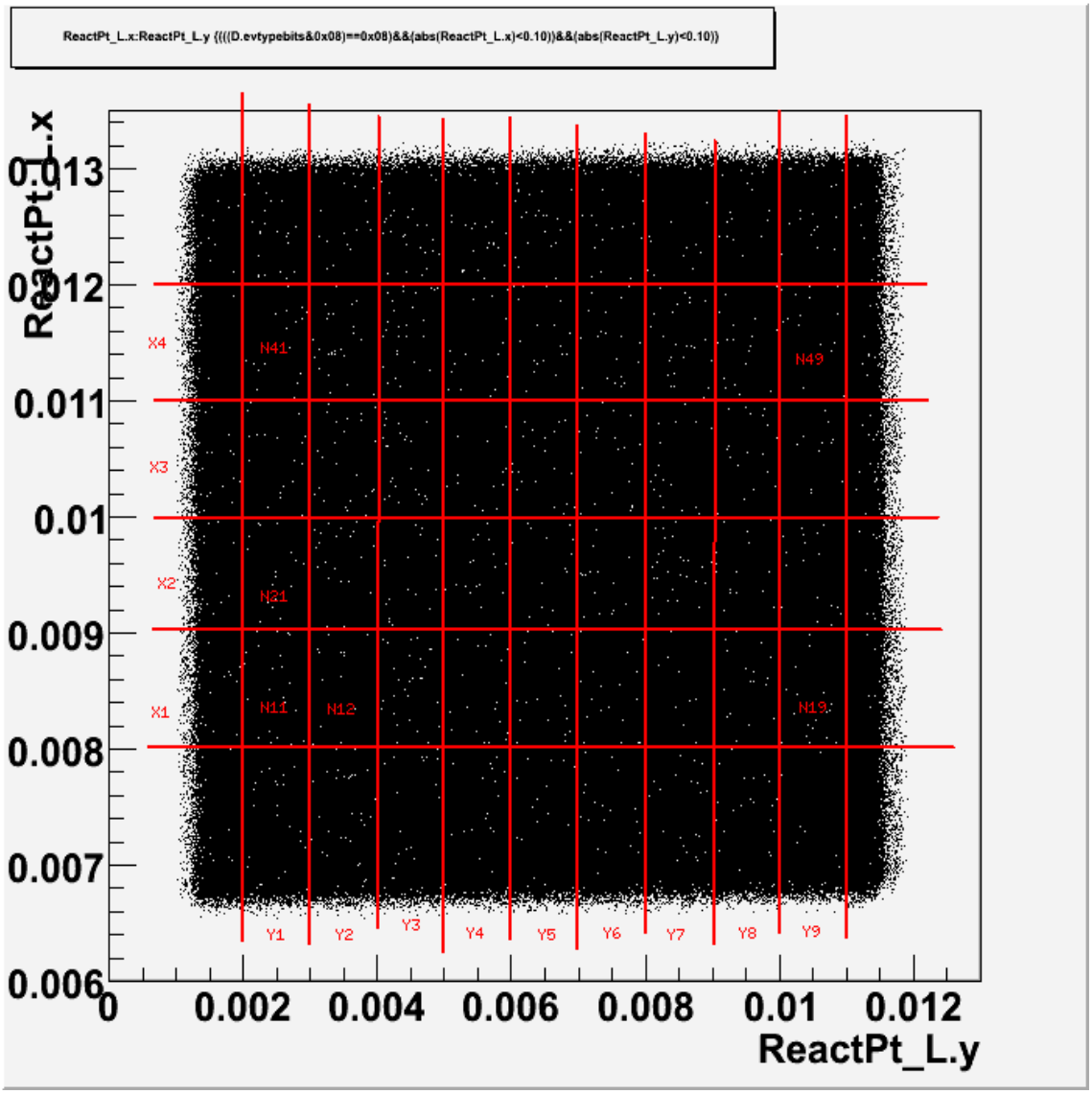

Figure 4.2: Raster pattern of kin02, run 3105, graphite with matrix for regional cuts shown.

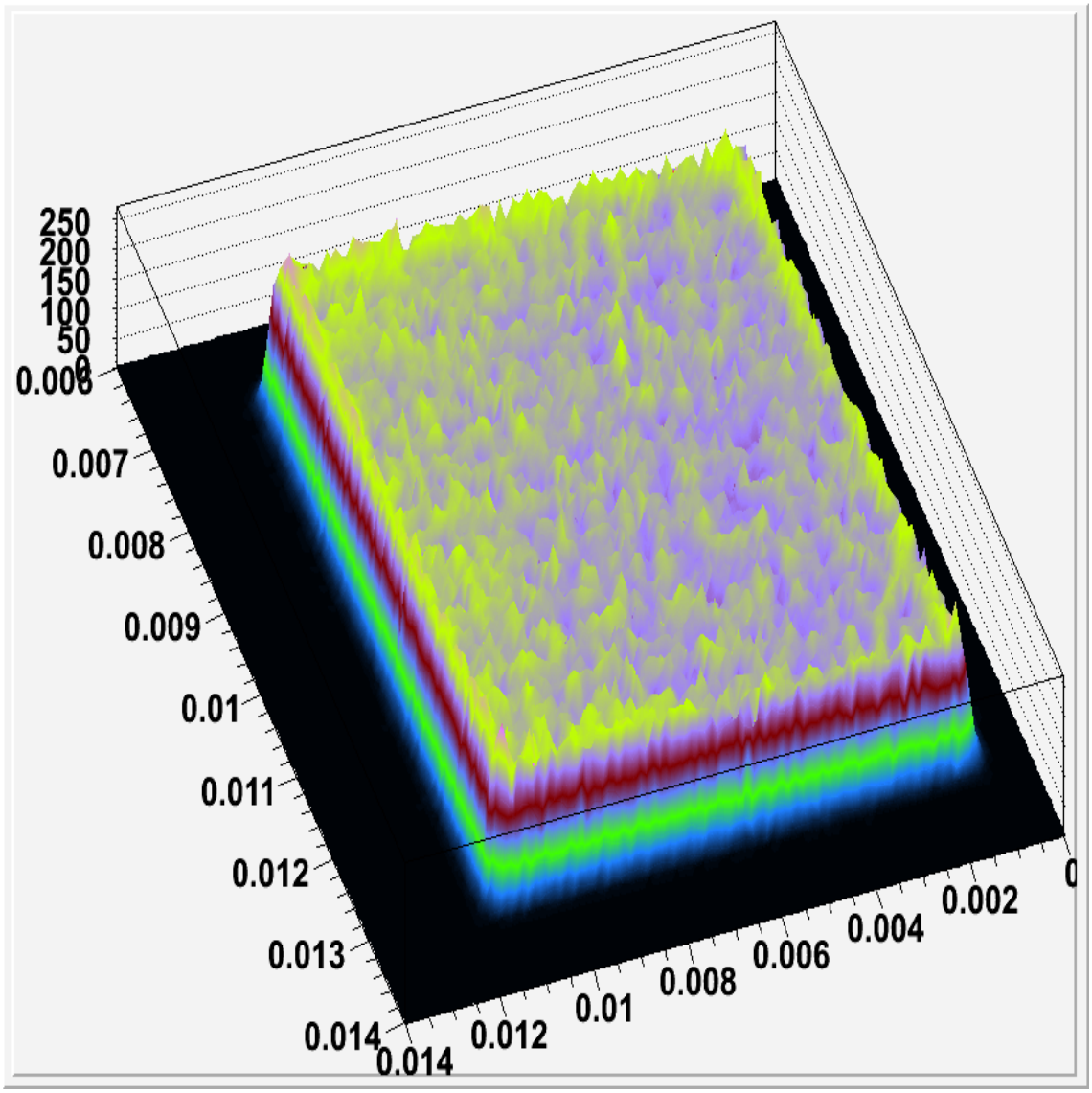

Figure 4.3: 3d raster pattern of kin02, run 3105, graphite.

Chapter 5

Radiative Losses

The graphite singles spectrum can be used to deduce the corresponding carbon singles spectrum from the metal/diamond sandwich. The correspondence will be a first approximation since the diamond foils straddle the heavy metal foils. It would not be possible to do the simulation with this exact geometry because we do not have a spectrum from carbon after the electron beam has passed through the metal. However, electrons from the upstream and downstream foils must all have passed through the metal, either after scattering in the upstream foil or from the downstream foil after the beam has passed through the metal. The simulation described here compares the measured graphite spectrum to that spectrum after it has passed through the metal foil. Since the other sources of radiation, such as the kapton windows, titanium windows and air, are already included in the graphite spectrum, for the metal simulation all windows are removed so only the effect of the metal is included. Figures 5.1, 5.2 and 5.3 show the measured graphite spectrum(solid curve) and the the simulated graphite spectrum(dashed curves) after passing through the metal foils tilted at 31deg. The spectrometer acceptance cuts off the dp spectrum below -0.03 so the comparison between graphite and graphite+metal can be made for $-0.03 \leq dp \leq +0.05$. The ratio of areas for this interval gives the factor to be applied to the carbon contribution from the diamond foils compared to the counts from pure graphite. One million electrons initially distributed over the measured graphite spectrum were used to generate the spectra after passing through the foils.

There are significant radiative losses for these heavy metal targets as shown in table 5.1. These radiative losses must be included properly to subtract the contribution of the diamond foils to the total rate seen from the heavy metal targets.

	bismuth	thin lead	thick lead
thickness(mm)	0.203	0.17	0.5
rad. loss factor	0.757	0.789	0.514

Table 5.1: The radiative loss factor is to be multiplied against the normalized graphite yield to account for radiative losses of events from the diamond foils due to the heavy metal foil.

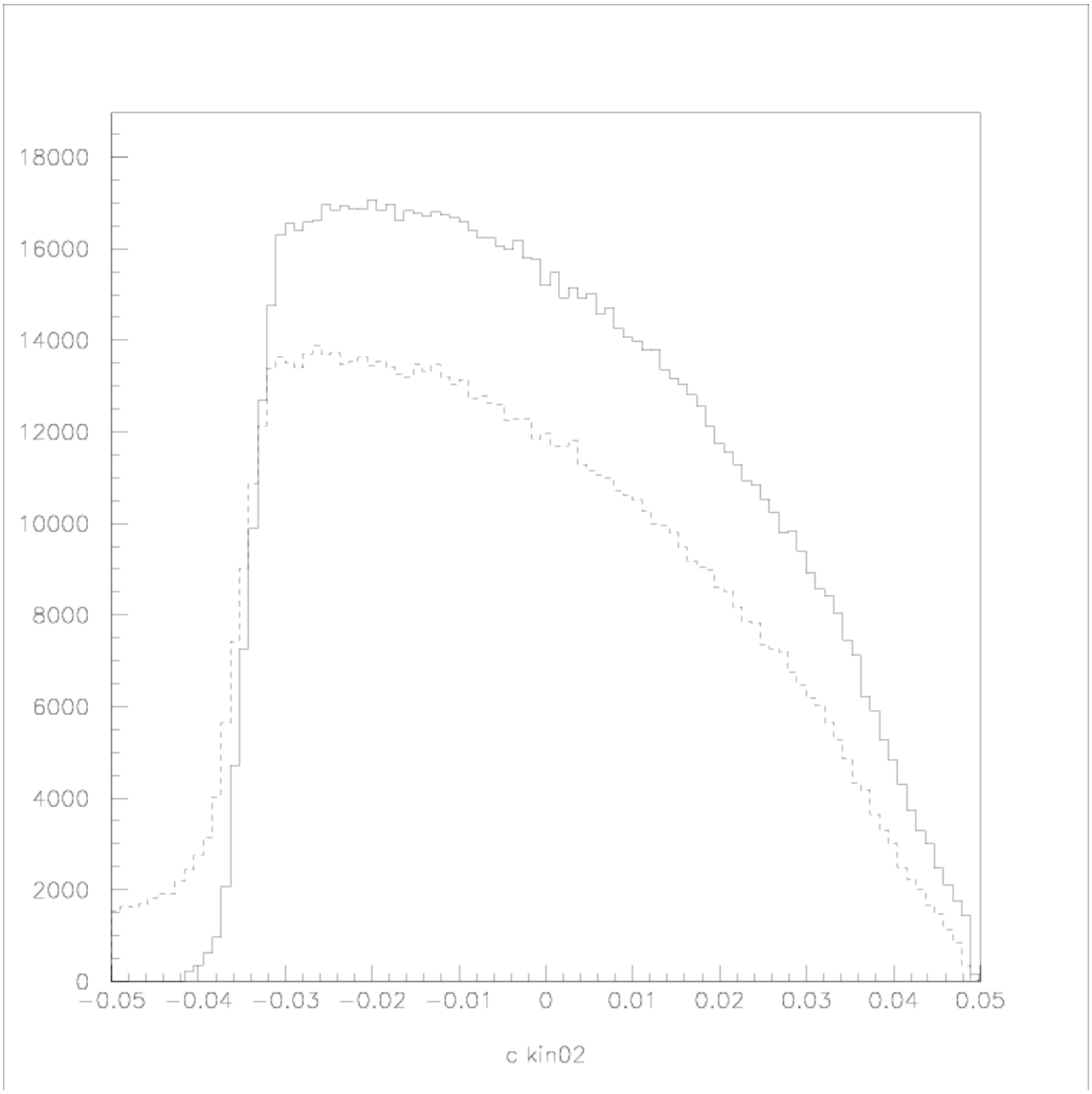

Figure 5.1: The solid curve is the measured graphite spectrum. The dashed curve shows the geant predicted spectrum from the diamond foils for the 0.203mm thick bismuth target tilted at 31 degrees. One million electrons distributed over the graphite spectrum are used.

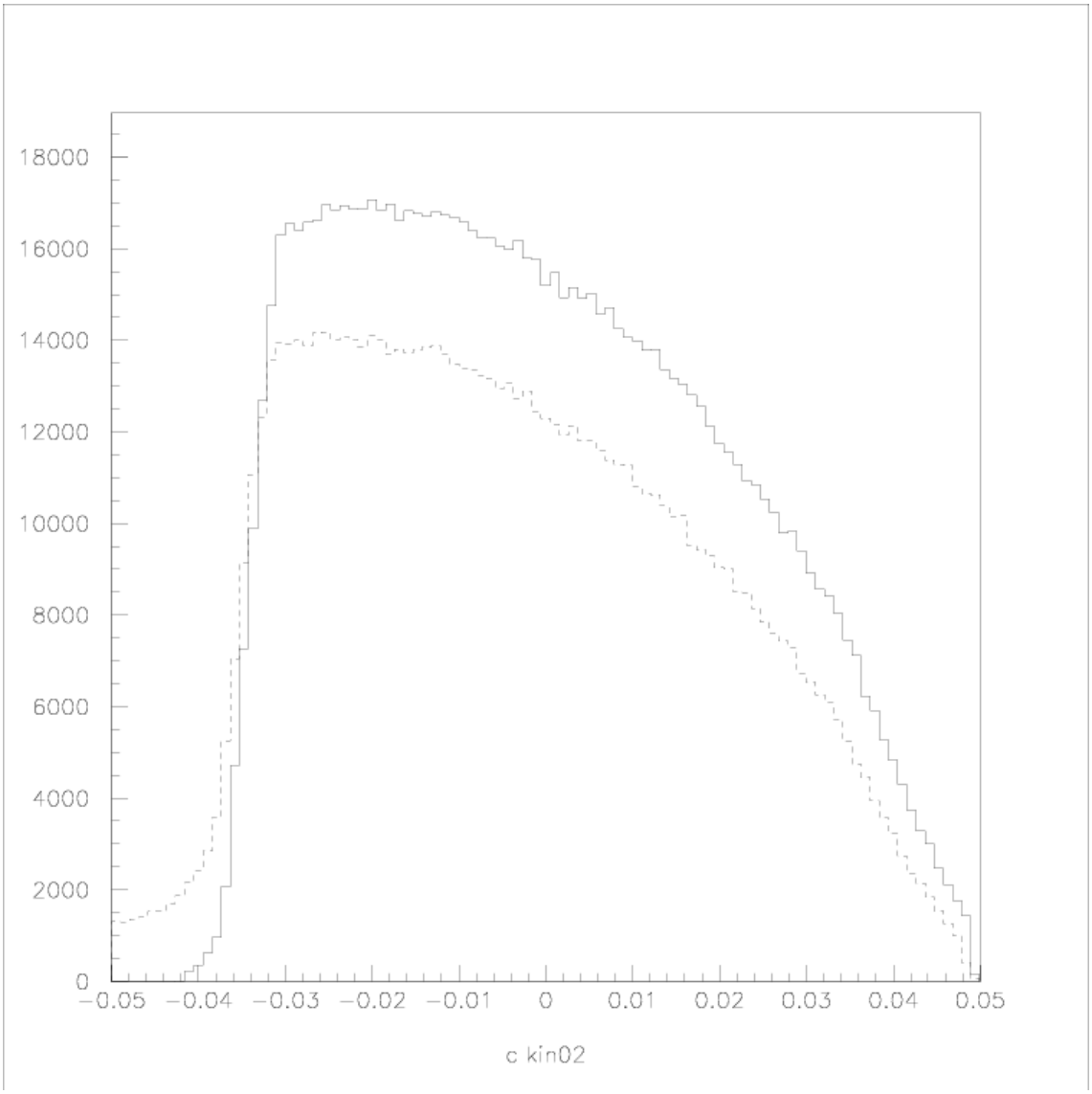

Figure 5.2: The solid curve is the measured graphite spectrum. The dashed curve shows the geant predicted spectrum from the diamond foils for the 0.17mm thin lead target tilted at 31 degrees. One million electrons distributed over the graphite spectrum are used.

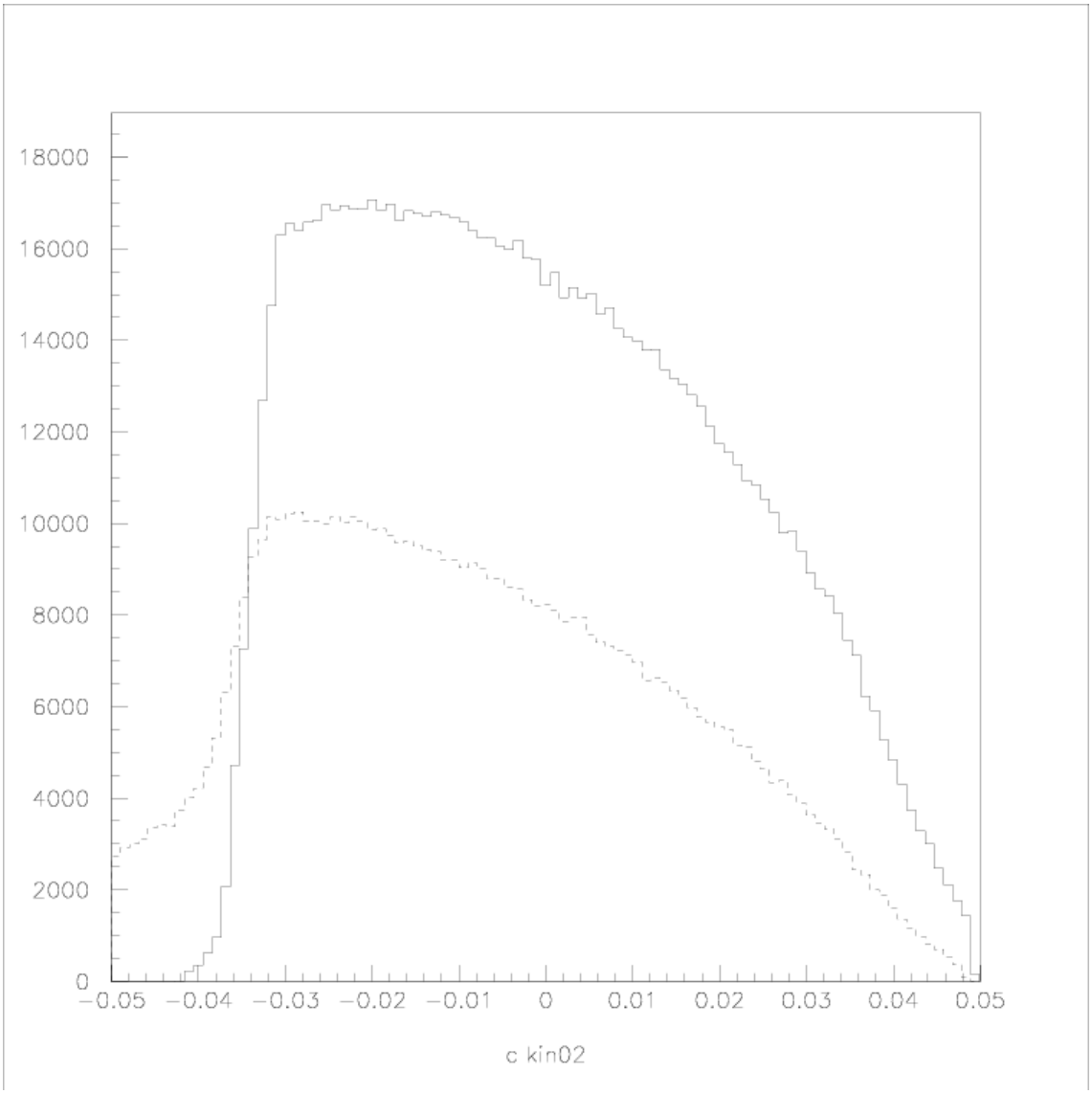

Figure 5.3: The solid curve is the measured graphite spectrum. The dashed curve shows the geant predicted spectrum from the diamond folis for the 0.5mm thick lead target tilted at 31 degrees.One million electrons distributed over the graphite spectrum are used.

Chapter 6

Thin Lead data

A picture of the disassembled thin lead target after the run is seen in figure 6.1. The raster pattern is visible as a discoloration but no significant distortion of the target morphology is seen.

The normalized yield for the thin lead target in kin02 using the full raster pattern is displayed in table 6.1. The same yield for a tighter cut on the raster pattern is displayed in table 6.2. The carbon background is subtracted based on the graphite yield and the diamond thickness. In the case of the lead target the graphite yield is also modified by a factor of 0.789 to account for the radiative loss of scattered electrons due to the lead foils.

The normalized yield for the lead target is plotted for two different size raster cuts shown in figure 6.2. The first few runs, 3111, 3112, 3113 and 3114 are for currents of 10 to 20 μA.

A check was made during kin02 for the effect of beam current on the distribution of counts within the raster pattern for the 36 regions shown in figure 4.2, cutsx(0.008,0.12), cutsy(0.002,0.011). The matrices of counts for an early run on the thin lead target, r3111, $10\mu A$ and a latter run, r3128, $56\mu A$ are shown in tables 6.3 and 6.4. No significant difference in the target profile was detected over these two ranges of beam current.

The LHRS normalized counting rate for kin08, kin09, kin10 and kin11 is shown in table 6.5.

kin	run number	target	current μ A	raster fraction	LHRS singles, normalized $\times 10^7$
kin01	3232	Pb-on	9.8	1	10.27
	3233	Pb-on	30	1	10.35
	3234	Pb-on	58	1	10.50
	3365	Pb-on	47	1	10.56
kin02	3111	Pb-on	10	1	10.17
	3112	Pb-on	20	1	10.22
	3113	Pb-on	20	1	10.13
	3114	Pb-on	20	1	10.22
	3115	Pb-on	30	1	10.18
	3116	Pb-on	30	1	10.20
	3117	Pb-on	37	1	10.22
	3118	Pb-on	50	1	10.52
	3119	Pb-on	31	1	10.31
	3120	Pb-on	50	1	10.25
	3121	Pb-on	59	1	10.45
	3122	Pb-on	57	1	11.32
	3123	Pb-on	54	1	10.30
	3124	Pb-on	57	1	11.22
	3125	Pb-on	7	1	10.14
	3126	Pb-on	60	1	10.37
	3127	Pb-on	52	1	11.28
	3128	Pb-on	56	1	11.28
	3129	Pb-on	59	1	11.27
	3130	Pb-on	55	1	11.25
	3131	Pb-on	37	1	10.39
	3132	Pb-on	20	1	10.45
kin03	3307	Pb-on	59	1	10.66

Table 6.1: Normalized LHRS singles counts for the thin lead target, kin01, kin02 and kin03. Full raster pattern used.

kin	run number	target	current μ A	raster fraction	LHRS singles, normalized $\times 10^7$
kin01	3232	Pb-on	9.8	0.303	10.62
	3233	Pb-on	30	0.303	10.86
	3234	Pb-on	58	0.303	11.72
kin02	3111	Pb-on	10	0.303	10.34
	3112	Pb-on	20	0.303	10.46
	3113	Pb-on	20	0.303	10.21
	3114	Pb-on	20	0.303	10.25
	3115	Pb-on	30	0.303	10.32
	3116	Pb-on	30	0.303	10.24
	3117	Pb-on	37	0.303	10.26
	3118	Pb-on	50	0.303	11.04
	3119	Pb-on	31	0.303	10.26
	3120	Pb-on	50	0.303	10.42
	3121	Pb-on	59	0.303	11.36
	3122	Pb-on	57	0.303	11.55
	3123	Pb-on	54	0.303	10.50
	3124	Pb-on	57	0.303	11.36
	3125	Pb-on	7	0.303	10.71
	3126	Pb-on	60	0.303	9.002
	3127	Pb-on	52	0.303	13.21
	3128	Pb-on	56	0.303	13.15
	3129	Pb-on	59	0.303	11.56
	3130	Pb-on	55	0.303	11.40
	3131	Pb-on	37	0.303	10.56
	3132	Pb-on	20	0.303	10.75

Table 6.2: Normalized LHRS singles counts for the thin lead target, kin01 and kin02. Raster pattern cutsx(0.008,0.012),cutsy(0.004,0.009) used.

```
Pb,kin02,r3111,10uA, cutsx(0.008,0.12), cutsy(0.002,0.011)
0.938 0.969 0.957 1.012 0.968 1.017 1.009 1.034 1.047
0.973 0.995 0.987 1.005 0.997 0.985 1.019 1.011 1.038
0.982 0.973 0.983 1.011 0.998 1.025 1.025 1.023 1.045
0.986 0.955 0.956 1.019 1.012 0.990 1.012 1.011 1.030

avg = 3800.
standard deviation = 104.
sqrt(avg) = 62. fractional statistical error = 0.016
```

Table 6.3: Raster pattern matrix for the thin lead target, I=10μA, run3111, kin02.

```
Pb,kin02, r3128,56uA, cutsx(0.008,0.12), cutsy(0.002,0.011)
0.955 0.986 0.986 0.968 0.981 1.007 1.021 1.013 1.035
0.965 0.973 0.999 0.975 0.994 1.007 1.036 1.042 1.056
1.000 0.945 0.957 0.998 0.984 1.020 0.993 1.013 1.027
1.005 0.964 0.991 0.974 0.961 1.027 1.021 1.040 1.080

avg = 3675
standard deviation = 114
sqrt(avg) = 61
 fractional statistical error = 0.016
```

Table 6.4: Raster pattern matrix for the thin lead target, I=56μA, run3128.

Figure 6.1: Thin lead target(0.17mm) after exposure to the beam. Discoloration on target surface shows the raster pattern. No distortion of the lead foil is seen in the visual inspection.

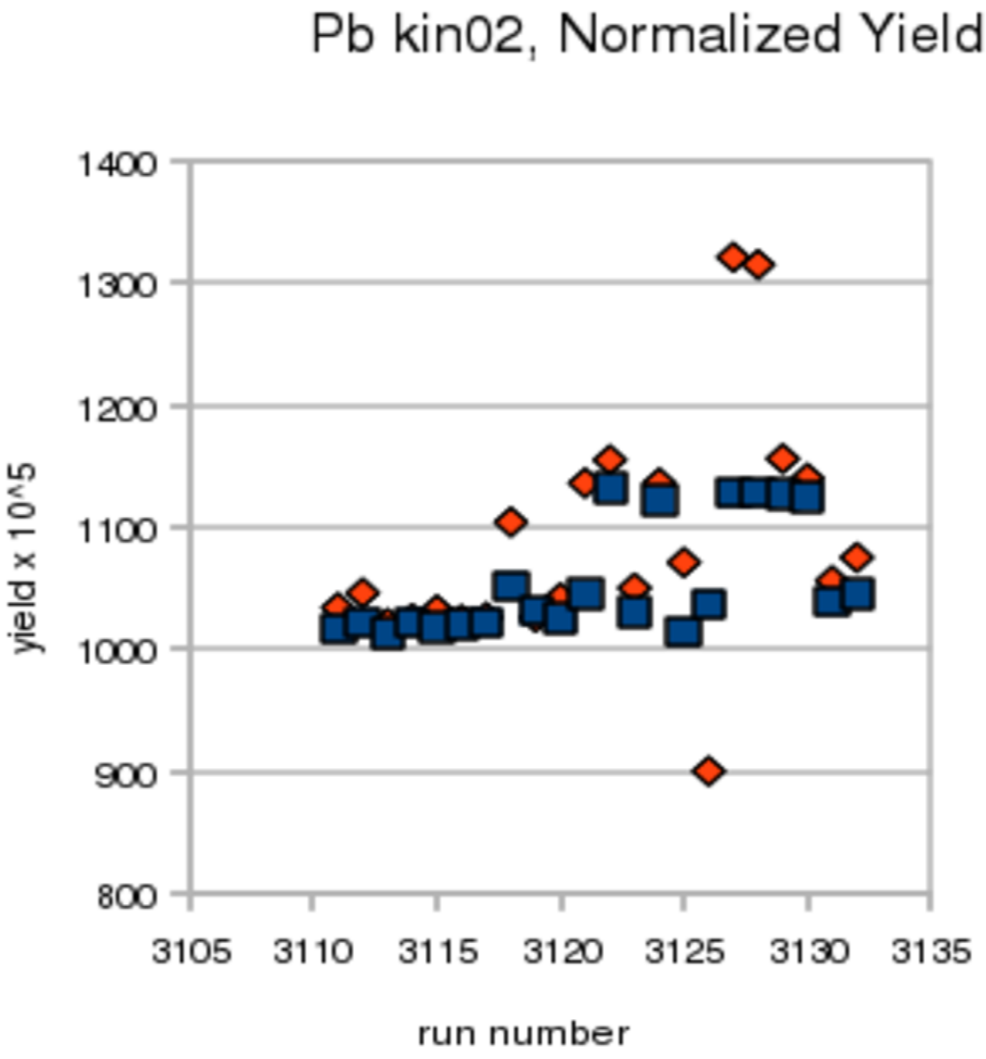

Figure 6.2: Normalized yield per Coulomb for Pb kin02. The diamonds are for a small raster cut, cutsx(0.008,0.012),cutsy(0.004,0.009)(raster fraction =0.303). The squares are for the full raster pattern.

kin	run number	target	current μ A	raster fraction	LHRS singles, normalized $\times 10^7$
kin08	3341	Pb-on	69	1	10.49
	3342	Pb-on	70	1	10.50
	3343	Pb-on	71	1	10.51
	3351	Pb-on	70	1	10.52
	3352	Pb-on	73	1	10.53
	3353	Pb-on	77	1	10.55
	3354	Pb-on	56	1	10.53
kin09	3367	Pb-on	79	1	10.97
	3368	Pb-on	44	1	10.85
	3369	Pb-on	12	1	10.64
	3370	Pb-on	65	1	10.81
	3371	Pb-on	76	1	10.80
	3372	Pb-on	80	1	10.83
	3373	Pb-on	78	1	10.83
kin10	3355	Pb-on	77	1	10.53
	3356	Pb-on	77	1	10.50
	3357	Pb-on	79	1	10.63
	3358	Pb-on	76	1	10.65
	3359	Pb-on	70	1	10.67
	3360	Pb-on	71	1	10.66
	3361	Pb-on	69	1	10.64
	3362	Pb-on	79	1	10.70
	3363	Pb-on	73	1	10.67
	3364	Pb-on	66	1	10.65
kin11	3300	Pb-on	2.4	1	10.46
	3301	Pb-on	48	1	10.67
	3302	Pb-on	59	1	10.71
	3303	Pb-on	59	1	10.70
	3304	Pb-on	59	1	10.71
	3305	Pb-on	59	1	10.72
	3306	Pb-on	59	1	10.67

Table 6.5: Normalized LHRS singles counts for the thin lead target, kin08, kin09, kin10 and kin11. Full raster pattern is used.

Chapter 7

Bismuth data

A picture of the disassembled bismuth target after the run is seen in figure 7.1. The raster pattern is visible as a discoloration but no significant distortion of the target morphology is seen.

The bismuth target was never exposed to low current running. Data are available at $59\mu A$ for runs 3313 through 3336 for kin04. The matrix of counts over the 36 regions in cutsx(0.008,0.12), cutsy(0.002,0.011) is shown in table 7.1 for run 3336. The count rate per region is as smooth as that for the graphite target and the lead target.

The normalized yield for the bismuth target using the full raster pattern is displayed in table 7.2. The same yield for a tighter cut on the raster pattern is displayed in table 7.3. The carbon background is subtracted based on the graphite yield and the diamond thickness. In the case of the bismuth target the graphite yield is also modified by a factor of 0.757 to account for the radiative loss of scattered electrons due to the bismuth foil.

Since the thin bismuth and thin lead targets were stable during run 2 it is interesting to check if the expected counting rate ratio according to a simple

```
Bismuth, kin04, run 3336, 59uA, cutsx(0.008,0.12), cutsy(0.002,0.011)
0.998 0.999 0.994 1.005 0.990 1.035 0.986 1.018 1.014
0.990 0.976 0.972 1.000 0.997 0.984 0.994 1.008 1.026
1.016 0.997 1.008 0.980 1.001 0.993 1.002 1.020 1.019
0.990 0.996 0.970 0.983 0.989 0.966 1.006 1.036 1.038

avg = 5416
standard deviation = 99
sqrt(avg) = 74
 fractional statistical error = 0.014
```

Table 7.1: Raster pattern matrix for the bismuth target, I=59μA, run 3336.

kin	run number	target	current μ A	raster fraction	LHRS singles, normalized $\times 10^7$
kin04	3313	Bi-on	59	1	11.08
	3314	Bi-on	59	1	11.03
	3315	Bi-on	59	1	11.04
	3316	Bi-on	59	1	11.03
	3317	Bi-on	59	1	11.05
	3318	Bi-on	59	1	11.06
	3334	Bi-on	59	1	11.03
	3335	Bi-on	59	1	11.01
	3336	Bi-on	59	1	11.01

Table 7.2: Normalized LHRS singles counts for the bismuth target, kin04. Full raster pattern used.

kin	run number	target	current μ A	raster fraction	LHRS singles, normalized $\times 10^7$
kin04	3313	Bi-on	59	0.306	11.02
	3314	Bi-on	59	0.306	10.91
	3315	Bi-on	59	0.306	10.93
	3316	Bi-on	59	0.306	11.01
	3317	Bi-on	59	0.306	10.91
	3318	Bi-on	59	0.306	11.07
	3334	Bi-on	59	0.306	10.97
	3335	Bi-on	59	0.306	10.92
	3336	Bi-on	59	0.306	10.98

Table 7.3: Normalized LHRS singles counts for the bismuth target, kin04. Raster pattern cutsx(0.008,0.012),cutsy(0.004,0.009).

model is followed. Since the LHRS was set for quasielatic scattering a first approximation is to assume that the rate of electron scattering is proportional to the number of protons. Using the measured thicknesses of these targets we can determine the number of bismuth or lead nuclei per unit area. From table 3.3 we determine that $\rho_{Pb} = 5.80 \times 10^{20}/cm^2$ and $\rho_{Bi} = 6.71 \times 10^{20}/cm^2$, for the 30° target angle. We also take account of the difference in radiative losses for these two targets from table 5.1. So the ratio of normalized counts from this simple model is then

$$counts_{Bi}/counts_{Pb} = (6.72/5.80) * (83/82) * (0.757/0.789) = 1.12 \qquad (7.1)$$

We compare the simple model to the measured ratio coming from the average for bismuth(table 7.2) and the $10\mu A$ run 3111(table 6.1).

$$counts_{Bi}/counts_{Pb} = 11.04/10.17 = 1.09 \qquad (7.2)$$

The ratios agree to within 3% and this gives us confidence that for run 1, where the bismuth target was seriously damaged, that comparing lead singles and bismuth singles rates is a valid measure of relative target thicknesses.

Figure 7.1: Bismuth target(0.203mm) after exposure to the beam. Discoloration on target surface is the raster pattern. Visual inspection of the bismuth target shows no significant change in the target's structure.

Chapter 8

Thick Lead data

A picture of the disassembled thick lead target after the run is seen in figure 8.1. The target appears to have been cratered by the beam with an indentation in the raster pattern surround by a ridge.

The normalized counting rate for the thick lead target, kin01 and kin02, is displayed in table 8.1.

The normalized counting rate for kin08, kin09 and kin10 for the thick lead target is in table 8.2

The raster pattern for the first runs on the thick lead target, r3133 and r3134 at $10\mu A$ and $14\mu A$ is shown in table 8.3. The distribution is uniform within statistical fluctuations. The raster pattern for run3310, the last run on the thick lead target, is shown in table 8.4. Within the raster pattern there is not a statistically significant deviation from a uniform distribution.

If we compare the normalized counting rates for the $10\mu A$ initial exposures between the thin(r3111,table 6.1) and thick(r3133,table 8.1) lead targets we find a ratio $(thick/thin)_{counts} = 22.22/10.17 = 2.18$. The ratio of target thicknesses is $(thick/thin)_{mm} = 0.5/0.17 = 2.94$. However, we should be correcting for radiative losses comparing these two different targets. The best we can do in this case is to see how the graphite spectrum is changed for the two cases of lead thicknesses. From table 5.1 the radiatively corrected ratio should be $(thick/thin)_{counts\_radiative} = 2.18 * (0.789/0.514) = 3.35$. The ratio of radiatively corrected counts is 14% larger than the simple ratio of target thicknesses. It is not clear if this excess is actually due to a change in target thickness or an incorrect handling of radiative effects. From figure 8.1 it is clear that the thick lead target's surface was altered by the beam. From tables 8.3 and 8.4 we see no change in the counting rates over the raster pattern between initial low current exposure and the last high current exposure to the beam. The possibility that the thick lead target is actually thicker by 14% than the original measured value is not unreasonable. We know from run 1 that the bismuth target was seriously damaged by the beam and the thickness deduced from electron scattering was about 45% larger than the initial target thickness(See section 9.2 of the first report on run 1.).

kin	run number	target	current μ A	raster fraction	LHRS singles, normalized $\times 10^7$
kin01	3310	Pb-on	58	1	25.45
kin02	3133	Pb-on	10	1	22.22
	3134	Pb-on	14	1	22.18
	3135	Pb-on	28	1	22.12
	3136	Pb-on	37	1	22.30
	3137	Pb-on	50	1	22.29
	3138	Pb-on	60	1	22.29
	3139	Pb-on	18	1	22.65
	3142	Pb-on	9	1	22.21
	3148	Pb-on	56	1	22.65
	3149	Pb-on	58	1	22.79
	3150	Pb-on	59	1	22.85

Table 8.1: Normalized LHRS singles counts for the thick lead target, kin01 and kin02. Full raster pattern used.

kin	run number	target	current μ A	raster fraction	LHRS singles, normalized $\times 10^7$
kin08	3151	Pb-on	48	1	22.63
	3153	Pb-on	54	1	22.76
	3169	Pb-on	49	1	24.24
	3170	Pb-on	58	1	24.37
	3171	Pb-on	53	1	24.33
kin09	3267	Pb-on	44	1	26.18
	3268	Pb-on	44	1	26.22
	3269	Pb-on	44	1	25.89
	3270	Pb-on	44	1	26.58
	3271	Pb-on	44	1	26.50
	3272	Pb-on	44	1	26.35
kin10	3205	Pb-on	28	1	24.46
	3206	Pb-on	47	1	24.59
	3207	Pb-on	56	1	24.63
	3208	Pb-on	60	1	24.61
	3209	Pb-on	56	1	24.67
	3217	Pb-on	53	1	24.72
	3218	Pb-on	51	1	24.67
	3219	Pb-on	54	1	24.60
	3220	Pb-on	53	1	24.70
	3221	Pb-on	59	1	24.71

Table 8.2: Normalized LHRS singles counts for the thick lead target, kin08, kin09 and kin10. Full raster pattern used.

Pb-thick runs 3133+3134, 10uA and 14uA, cutsx(0.008,0.12), cutsy(0.002,0.11)								
1.005	0.964	1.021	1.030	0.967	1.046	1.030	1.038	1.010
0.978	0.992	0.958	0.970	0.919	0.975	1.018	0.989	1.068
1.021	0.973	0.968	1.040	0.991	0.996	0.980	1.092	1.043
0.990	0.961	0.979	1.005	0.960	1.019	0.948	1.040	1.015
avg = 1022.444 stddev = 37.281 fract stddev = 0.036								

Table 8.3: Thick lead target, r3133+r3134 combined raster pattern for the first few low current runs, $10\mu A$ and $14\mu A$. There is not a statistically significant difference from a uniform distribution within the raster pattern.

Pb-thick, kin01, 60uA, r3310 cutsx(0.008,0.12), cutsy(0.002,0.11)								
0.971	0.858	1.046	1.046	1.059	1.089	0.993	1.094	1.024
0.945	0.980	1.006	0.993	1.081	1.006	1.054	0.879	1.006
0.976	1.033	1.006	0.954	0.932	1.041	1.024	1.085	1.098
1.002	0.849	0.993	1.054	0.923	0.989	1.006	0.963	0.941
avg = 228.556 stddev = 14.364 fract stddev = 0.063								

Table 8.4: Thick lead target, r3310 raster pattern. This is the last run on the thick lead target. There is not a statistically significant difference from a uniform distribution within the raster pattern.

Figure 8.1: Thick lead target(0.5mm) after exposure to the beam. Visual inspection shows a significant change in the target's surface. There appears an indentation in the raster pattern with a ridge around the crater.